

Effect of the unbonding materials on the mechanic behavior of all-steel buckling-restrained braces



Quan Chen ^a, Chun-Lin Wang ^{a,*}, Shaoping Meng ^a, Bin Zeng ^b

^aKey Laboratory of Concrete and Prestressed Concrete Structures of the Ministry of Education, Southeast University, Nanjing 210096, China

^bCentral Research Institute of Building and Construction, MCC Group, Beijing 100088, China

ARTICLE INFO

Article history:

Received 15 June 2015

Revised 15 December 2015

Accepted 17 December 2015

ABSTRACT

Seven all-steel buckling-restrained braces (BRBs) were tested under cyclic loading to investigate the effect of the unbonding materials on the performance of BRBs, via the employment of a layer of 1-mm thick butyl rubber or pure air gap between the core plate and the restraining system. Test results indicate that all the BRBs exhibited rather well energy dissipation capacities and sustained cumulative plastic deformations over 1000 times the yield strain. However, significantly higher compression strength adjustment factor β was developed for the specimens without the unbonding materials, due to the gradually increasing friction force and the jamming between the end of the core plate and the restraining members. Moreover, the gradually increasing friction force and the jamming also induced the considerably nonuniform residual deformation for the specimens without the unbonding materials both observed in the test and the finite element models. Especially, for high performance BRBs with relatively long yielding segment and thin core plate, the unbonding materials are recommended to apply.

© 2015 Elsevier Ltd. All rights reserved.

1. Introduction

Concentrically braced frames have been prevalent owing to their large lateral stiffness with less lateral displacement under severe earthquake at a low cost. However, damages of the braces due to buckling have been frequently found under severe earthquakes (e.g., the 1994 Northridge earthquake [1]), which limited the ductility and energy dissipation capacity of the frames. Alternatively, buckling-restrained braced frames (BRBFs), with both high lateral stiffness and stable hysteretic properties, have been increasingly popular among designers. Buckling-restrained brace (BRB) is a special type of brace with global buckling inhibited by an appropriate restraining system, which implies the compression hysteretic behavior similar to the tension hysteretic behavior.

In the recent decades, a number of studies have been conducted both at the component and frame levels to develop different types of BRBs for seismic hazard mitigation. At the component level, Black et al. [2] experimentally verified the results of theoretical predictions on the structural stability of the braces, and validate the inelastic capacity of the braces under severe earthquake demands. Further, Wang et al. [3] developed a type of aluminum

alloy buckling-restrained braces to enhance the durability of BRBs in bridge engineering. In order to improve the low-cycle fatigue performance of BRBs, Wang et al. [4] employed toe-finished method in the welds between the ribs and the core plate. Besides, Zhao et al. [5] proposed and experimentally validated a global stability design method of BRBs considering the effect of end bending moment transfer. At the frame level, Wu et al. [6] provided design procedures to quantify the responses of BRBFs. In order to investigate the seismic behavior of the proposed BRBs, Tsai et al. [7,8] conducted pseudo-dynamic test on a full-scale 3-story 3-bay BRBF. Moreover, Sabelli et al. [9] and Fahnstock et al. [10] have predicted seismic response requirements for the design of BRBFs through a great amount of numerical analysis. Chen et al. [11] investigated the seismic demand of the BRBs which was employed to retrofit a steel arch bridge under severe earthquake.

Generally, the members used to restrain the buckling of the core plate in conventional BRBs are mortar or concrete cased in a steel tube. Between the core plate and the restraining members, unbonding materials are employed, not only to reduce the adhesion force between the core plate and the restraining members, but to provide the space for the expansion of the core plate under compression. Primarily, Wakabayashi et al. [12] conducted adhesion test on several materials, concluding that a layer of epoxy resin and silicon resin was the preferable unbonding materials. Until now, several unbonding materials (e.g. epoxy resin, silicon resin, vinyl tapes, etc.) have been widely employed in BRBs [13].

* Corresponding author at: School of Civil Engineering, Southeast University, Nanjing 210096, China.

E-mail address: chunlin@seu.edu.cn (C.-L. Wang).

Especially, Tsai et al. [13] tested ten BRBs with different unbonding materials and found that a 2-mm thick silicon rubber sheet had the least axial load difference for the proposed BRB. Moreover, Tsai et al. [14] tested four BRB specimens with different unbonding materials (high density styrofoam sheet, chloroprene rubber, rubber sheet and silicone sheet), and compared their hysteretic properties and cost effect.

However, it is time-consuming to pour and cure the concrete or mortar in conventional BRBs, and local buckling was observed due to the crush of the concrete or mortar in certain experiments [15,16]. Therefore, different types of BRBs with restraining members mainly made of steel, designated as all-steel BRBs, have been proposed by several researchers in the last few years. Since the adhesion between the steel core plate and the steel restraining members is negligible and the space for the expansion of the core plate can be provided by controlling the dimension of the steel restraining members, the unbonding materials seem not indispensable in all-steel BRBs. But several types of lubricant were still employed on the surfaces of the core plate in all-steel BRBs [17,18]. Recently, in the experiment presented in the literature [19], a small air gap was used between the core plate and the steel restraining tubes instead of the unbonding materials, which did not affect the cyclic behavior of the proposed BRB evidently. Della Corte et al. [20] also employed the air gap in all-steel BRBs and controlled the peak compression resistance through appropriate design of casting connections. Contradictory to those, Iwata [21] tested all-steel BRBs without the unbonding materials and found they finally fractured as a result of the continued progress of the plastic deformation. Likewise, Tremblay et al. [22] compared the performance of the conventional BRBs to all-steel BRBs without the unbonding materials, indicating that it is necessary to minimize the friction to develop the uniform strain in the core plate.

Since the role of the unbonding materials in all-steel BRBs is uncertain to date, more research needs to be conducted. In this article, two series of test specimens, comprised of seven all-steel BRB specimens, were designed to estimate the effect of the unbonding materials on the low-cycle fatigue performance of the all-steel BRBs. Different factors, including the existence of the unbonding materials, the testing protocol and the width of the in-plane gap, were employed in the test program for comparison.

2. High-mode buckling of the all-steel BRB

The employed all-steel BRB consists of a steel core plate, a pair of steel restraining plates and a pair of steel fillers, as shown in Fig. 1. Furthermore, the cross-sectional details of the BRB specimens are shown in Fig. 2, where the core plate is inserted between the pair of restraining plates connected by the high-strength bolts through two fillers on both sides of the core plate. Besides, a layer of 1-mm thick butyl sealant tape is adopted between the core plate and the restraining system, while for BRBs without the unbonding

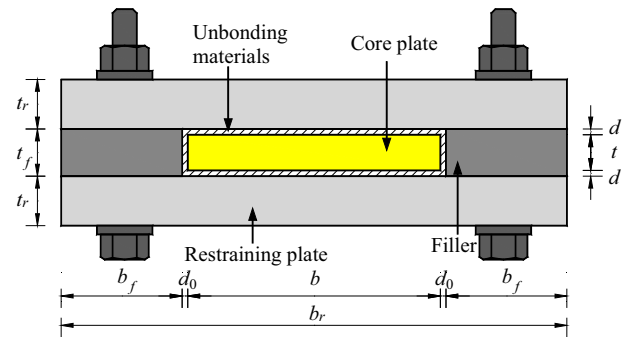


Fig. 2. Cross-sectional details. Note: b_r and t_r are the width and thickness of the restraining plate, respectively; b and t are the width and thickness of the yielding segment, respectively; b_f and t_f are the width and thickness of the fillers, respectively; d_0 and d are the widths of the in-plane and out-of-plane gap between the core plate and the restraining system, respectively.

materials, just 1-mm air gap is alternatively employed. To prevent the slip off the restraining members, the stopper is set at the center via enlarging the width of the core plate.

2.1. Weak-axis high-mode buckling wavelength

Even though global flexural buckling of the BRB under a large compressive strain can be prevented with sufficient stiffness of the restraining members [23], the weak-axis high-mode buckling of the core plate is still inevitable (Fig. 3). Euler formula has been employed to approximate the weak-axis high-mode buckling behavior, using the yield strength and the flexural stiffness of the core plate [19,24]. The buckling wave length was determined by Euler critical load without contact force, but researches have shown that the contact force may increase the critical load [25].

The buckling wave number (n) of a bi-laterally constrained elastic column has been estimated with Eq. (1) by solving the fourth-order, linearized differential equation for an Euler beam under increasing axial compression load [26], where P is the axial load and E is the elastic Young's modulus of the core plate, and L_y is the length of the constrained column (corresponding to the yielding segment of the core plate).

$$1 + 2n \leq \sqrt{\frac{3PL_y^2}{\pi^2 Ebt^3}} \leq 1 + 4n \quad (1)$$

where the left and right sides of the equation correspond to the upper and lower bounds of the number of waves respectively. Since the lateral deflection of the core plate is limited below the out-of-plane gap width ($d = 1$ mm), it is feasible to extend Eq. (1) to the elastic-plastic buckling behavior of the core plate based on the theory of elastic-plastic buckling developed by Shanley [27]. Replacing the Young's modulus E with the tangent modulus E_t in Eq. (1), the weak-axis high-mode buckling wavelength of the core plate l_w can be predicted as follows:

$$\frac{L_y}{\text{int}\left(\frac{1}{2}\sqrt{\frac{3PL_y^2}{\pi^2 E_t bt^3}} - \frac{1}{2}\right)} \leq l_w \leq \frac{L_y}{\text{int}\left(\frac{1}{4}\sqrt{\frac{3PL_y^2}{\pi^2 E_t bt^3}} - \frac{1}{4}\right)} \quad (2)$$

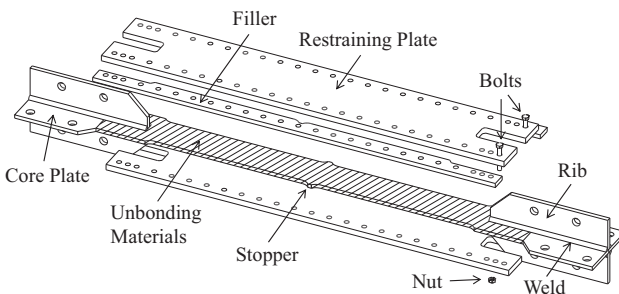


Fig. 1. Assemblage of the all-steel BRB.

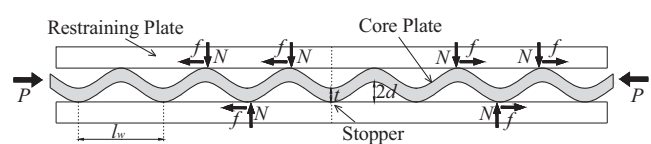


Fig. 3. Weak-axis high-mode buckling of the core plate.

where the function “int” denotes removing all decimal places from the number and leaving just the integer, and E_t is assumed as $0.02E$ for simplification hereinafter [17,28]. To evaluate Eq. (2), different values of wavelength from experiments [17,29] at certain strain amplitudes $\Delta\epsilon$ (maximum yielding segment deformation divided by its length at a cycle) are compared with the estimated bounds in Table 1. The lower bounds of l_w are more close to the experimental values against the upper bounds, for the friction force between the restraining members and the core plate could reduce the mobility of the buckle and concentrate line contact of the buckling in certain regions. Moreover, it is conservative to predict the contact force and the friction force between the restraining members and the core plate based on the lower bounds of the weak-axis high-mode buckling wavelength l_w , so the lower bounds are proposed in this paper as the theoretical buckling wavelength of the core plate:

$$l_w = \frac{L_y}{\text{int}\left(\frac{1}{2} \sqrt{\frac{3PL_y^2}{\pi^2 E_t b t^3}} - \frac{1}{2}\right)} \quad (3)$$

Additionally, experiment results have shown that the wavelength would remain almost unchanged if the subsequently applied compressive strain is smaller than the previous one, due to the accumulation of the plastic strain [17].

2.2. Normal contact force between the core plate and the restraining members

As shown in Fig. 3, when the core plate experiences weak-axis high-mode buckling under compression, normal contact forces develop between the restraining members and the crest of the core plate. According to previous studies [26], line contact other than point contact will form during high-mode buckling of the core plate. At this situation, only two concentrated contact forces exist at the two ends of contacted line, while in the rest part of the line there is no distributed contact force because the deflection curve is flat [30]. Based on the boundary conditions at line contact status, the contact force N can be calculated by solving the mechanical equilibrium of a buckling wave as [26,30]:

$$N = \frac{8d}{l_w} P \quad (4)$$

Moreover, Eq. (4) is consistent with the modified prediction formula of the contact force [29], which has been experimentally verified.

2.3. The compression strength adjustment factor

Generally, the maximum compressive force of BRBs P_{\max} is larger than the maximum tensile force T_{\max} in a loading cycle, on

account of both the Poisson's effect and the friction force between the core plate and the restraining members [31,32]. By assuming the constant volume of the yielding segment, the increase of the compressive force due to the Poisson's effect in terms of the tensile force β_1 can be calculated as:

$$\beta_1 = \frac{A_p}{A_T} \approx \frac{1 + \Delta\epsilon}{1 - \Delta\epsilon} \quad (5)$$

where A_p and A_T are the cross sectional areas of the yielding segment under compression and tensile, respectively. Based on the contact force N from Eq. (4), the increase of the compressive force due to the force in terms of the tensile force β_2 can be calculated as:

$$\beta_2 = \frac{T_{\max} + n\mu N}{T_{\max}} = \left(1 + n\mu \frac{8d}{l_w}\right) \quad (6)$$

where μ is the kinetic coefficient of friction between the core plate and the restraining system. In particular, n is the number of weak-axis waves, which is equal to L_y/l_w and used here to approximate the number of discrete contact regions between the restraining plate and half of the core plate in the longitudinal direction. In consideration of the two factors, the relationship between P_{\max} and T_{\max} can be predicted as:

$$P_{\max} = \beta T_{\max} = \frac{1 + \Delta\epsilon}{1 - \Delta\epsilon} \left(1 + n\mu \frac{8d}{l_w}\right) T_{\max} \quad (7)$$

where β is the compression strength adjustment factor at the strain amplitude of $\Delta\epsilon$. For simplification, the maximum tensile brace force T_{\max} can be predicted based on linear hardening constitutive equation as:

$$T_{\max} = [\sigma_y + E_t(\Delta\epsilon - \varepsilon_y)]bt \quad (8)$$

where σ_y and ε_y are the yield stress and strain of the core plate. The error between T_{\max} from the test and Eq. (8) is under 10% and only 3% at higher strain amplitude (2.0–3.0%).

At this point, the maximum compressive force P_{\max} and the buckling wavelength l_w can be calculated by solving Eqs. (3) and (7) simultaneously in principle, for a BRB with given geometry and material properties. To simplify, an alternative iteration procedure is employed to obtain P_{\max} and l_w by setting the maximum compressive force P_{\max} initially as the maximum tensile brace forces T_{\max} . Then the iteration procedure needs to be continued, with l_w in Eq. (7) and P_{\max} in Eq. (3) replaced by the updated ones respectively, until the maximum compressive force P_{\max} converges. Finally, P_{\max} and l_w can be obtained within acceptable errors, together with the compression strength adjustment factor β .

3. Test program

3.1. Specimens

As shown in Fig. 4, two series of specimens with different dimensions of the core plate were designed in the test. The steel core plate is composed of a yielding segment, steel core projections with ribs, and the transition segments between the projections and yielding segment. After undesirable failure was detected near the welds in Series I, specimens in Series II were designed with smaller width of the yielding segment ($b = 80$ mm) and longer length of the transition segment (90 mm). But the dimensions of the restraining plates were kept the same for the specimens in the two series, as shown in Fig. 5. The ribs were welds on the end of the core plates, which is marked with thick lines. As shown in Fig. 6, the stoppers were set at the center via enlarging the width of the core plate, inserting into the fillers. Specifically, Table 2 lists several measured geometric dimensions of the core plate and the restraining plates. Each specimen is designated as ‘x-yy’, where ‘x’ is the material

Table 1
Experimental and theoretical values of the wavelength l_w .

Specimen	$\Delta\epsilon$ (%)	l_w (mm)		
		Experiment	Lower bounds	Upper bounds
<i>Wu et al. [17]</i>				
W160t20-1	2.0	240	229	533
W160t20-2	3.5	241	229	533
W200t20-1	3.0	225	229	533
W200t20-2	1.5	324	267	533
W200t25-1	1.5	390	320	800
W200t25-2	2.0	290	267	533
<i>Genna and Gelfi [29]</i>				
5 + 0.25	2.0	74.6	56	122
7 + 0.25	2.0	101.8	93	187

Note: the tangent modulus is assumed to be 2% of the elastic Young's modulus [17].

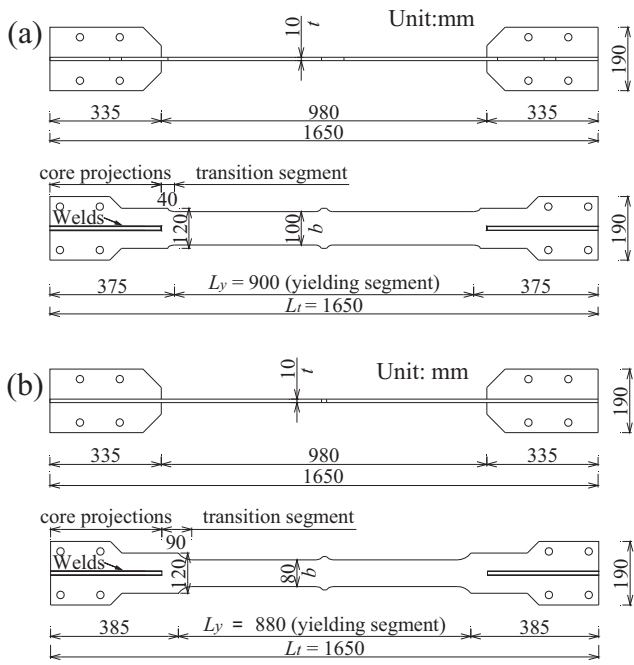


Fig. 4. Nominal dimension of the core plate: (a) Series I, (b) Series II. Note: L_t is the total length of the core plate; L_y is the length of yielding segment of the core plate.

employed between the core plate and the restraining members (A for air gap and U for unbonding materials), and 'yy' is the type of testing protocol. Exceptionally, specimen A-V2(3) is different from specimen A-V2 with larger in-plane gap width between the yielding segment and the filler d_0 , which is 3.0 mm in the parentheses. But the in-plane gap width between the transition segment and the filler d_1 for specimen A-V2(3) is kept at only 1.0 mm to avoid unfavorable rotation at the end, as shown in Fig. 6. Additionally, the height of the stopper h_s for specimen A-V2(3) is larger than that for specimen A-V2 (Fig. 6). The core plate is made of Q235B steel, and the results of the coupon test are listed in Table 3.

3.2. Test setup and testing protocol

The specimen was vertically mounted on the Material Test System (MTS) connected by high-strength bolts (Fig. 7). A hydraulic actuator, with a loading capacity of ± 1000 kN and a displacement capacity of ± 75 mm, was used for the cyclic loading, which was displacement-controlled via a linear variable displacement transducer mounted on the actuator.

Four different testing protocols were involved in the test, as shown in Fig. 8. At the beginning of each testing protocol, four cycles of loading with the strain amplitude $\Delta\varepsilon$ of $0.75\varepsilon_y$ were adopted to measure the initial axial stiffness of the specimens within the elastic stage and to examine the loading system. The subsequent loading phases of testing protocol V1 were a set of variable strain amplitude (VSA) loading with gradually increasing strain amplitudes $\Delta\varepsilon$ of 0.5%, 1.0%, 1.5%, 2.0%, 2.5% and 3.0% (two cycles at each strain amplitude), followed by the constant strain

amplitude (CSA) loading with strain amplitude of 2.0%. Likewise, the subsequent loading phases of testing protocol V2 were three identical sets of variable strain amplitude (VSA) loadings with gradually increasing strain amplitudes $\Delta\varepsilon$ of 0.5%, 1.0%, 1.5%, 2.0%, 2.5% and 3.0% (three cycles at 0.5%, two cycles at the other strain amplitudes), followed by the constant strain amplitude (CSA) loading with strain amplitude of 2.0%. Specifically, the three continuous sets of VSA loadings in testing protocol V2 are designated as VSA1, VSA2 and VSA3 hereinafter, respectively. More simply, the subsequent loading phases of testing protocols C1 and C2 were CSA loadings with strain amplitude $\Delta\varepsilon$ of 1.0% and 2.0%, respectively. Moreover, all the test protocols were continued until the failure of the specimens.

4. Test results

4.1. Hysteretic loops

The hysteretic loops of the seven specimens are presented in Figs. 9–14, where the failure of each specimen is marked with a red triangle. Meanwhile, the number of cycles before failure during the CSA loading is plotted in the lower right corner of the figures.

4.1.1. Specimens A-V1 and U-V1

The difference between the two specimens is merely whether employing the unbonding materials or not. As shown in Figs. 9 and 10, specimens A-V1 and U-V1 exhibited stable behavior without any sign of degradation before the 43rd and the 52nd cycles of the CSA loading, respectively. During the VSA loading, the two specimens demonstrated almost the same hysteretic behavior, when comparing Fig. 9(a) with Fig. 10(a). However, the hysterical loop of specimen A-V1 became apparently asymmetric with the development of the loading history in comparison with specimen U-V1 during the CSA loading. In other words, the compressive force became increasingly larger while the tensile force stayed stable, as shown in Fig. 9(b).

4.1.2. Specimens A-V2, U-V2 and A-V2(3)

Similar tendency was also detected when comparing specimen A-V2 with specimen U-V2 in Figs. 11 and 12. During the VSA1 loading, specimens A-V2 and U-V2 demonstrated similar hysteretic behavior, while the hysterical loop of specimen A-V2 became increasingly asymmetric during the following VSA and CSA loadings compared to specimen U-V2. Moreover, specimen U-V2 endured 38 cycles during the CSA loading before failure, which was considerably more than specimen A-V2 with only 7 cycles. Interestingly, specimen A-V2(3), the in-plane gap width d_0 of which is 3 mm, revealed more severe asymmetric hysteretic behavior (Fig. 13) even than specimen A-V2. The dramatically increased compression force is owing to the failure of the stopper [17,33], which has been observed after test. Besides, specimen A-V2(3) fractured rather early at the end of the VSA2 loading.

4.1.3. Specimens A-C1 and A-C2

As shown in Fig. 14(a), specimen A-C1 endured 249 cycles before fracture, and the asymmetric hysteretic behavior was also

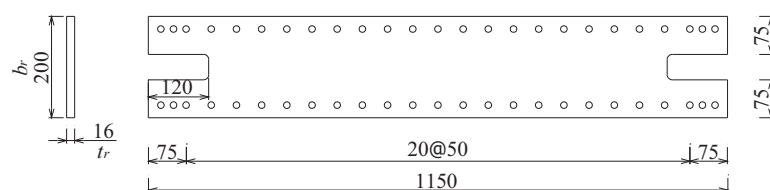


Fig. 5. Nominal dimension of the restraining plate.

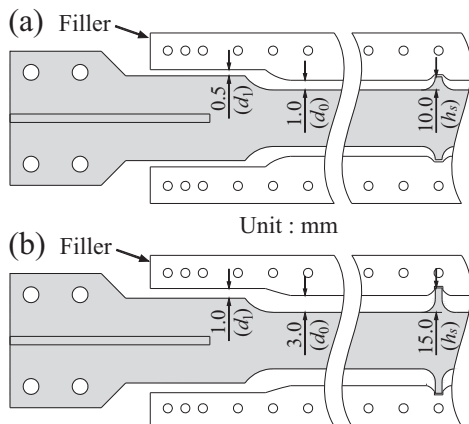


Fig. 6. In-plane design details of: (a) specimen A-V2, (b) specimen A-V2(3).

observed in specimen A-C1, but less significant than that in other specimens without the unbonding materials. Specimen A-C2 experienced substantial asymmetric hysteretic behavior, and failed after 44 loading cycles.

Overall, the specimens without the unbonding materials witnessed severe increases of the compressive force with the development of the loading history, compared to the specimens with the unbonding materials. Moreover, it is also revealed from the number of cycles before failure during the CSA loading that the specimens with the unbonding materials have higher low-cycle fatigue properties against the specimens without the unbonding materials. As listed in Table 4, the cumulative plastic deformation (CPD) capacities for all specimens are 3022, 3532, 2188, 5391, 1058, 5734, 2202 times the yield strain, which all outnumber 200 as required in AISC 2010 [34]. The great CPD capacities partly contribute to the employment of wire Electrical Discharge Machining (EDM) to cut the core plate, which has much higher accuracy than water jet cutting or laser cutting. What's more, no welds were included in the yielding segment. Therefore, stress concentration due to both cutting errors and welding is less likely to occur in the specimens, which hence improves the low-cycle fatigue properties of the specimens. Further, the CPD capacities for the specimens with the unbonding materials are higher than those for the specimens without the unbonding materials.

4.2. Failure modes

The failure modes for the seven specimens are presented in Fig. 15.

4.2.1. Specimens A-V1 and U-V1

As shown in Fig. 15(a)–(c), the core plate's failure for both specimens was induced by the crack initiating from the welds in the transition segment of the core plate near the rib. It is because that welding residual stress was expected to exist in the transition seg-

ment near the welds shown in Fig. 4, and hence the low-cyclic fatigue properties of the core plate near the welds are relatively low [4,35]. Further, since the width of the core plate was enlarged from 100 mm in the yielding segment to only 120 mm in the transition segment (Fig. 4), plastic strains were expected to develop in the transition segment near the welds, which is only 40 mm away from the yielding segment. As a result, cracks formed firstly in these regions. In addition, reduction of the section area was observed at the center of the core plate of specimen A-V1. Besides, a few subtle cracks were found near the stopper in specimen U-V1.

4.2.2. Specimens A-V2, U-V2 and A-V2(3)

To avoid the failure in the transition segment of the core plate, two geometry modifications in Series II (comparing Fig. 4 (a) and (b)) are noted: (1) the width of the yielding segment of the specimens was reduced from 100 mm to 80 mm, while the width of the transition segment near the welds was still kept as 120 mm; (2) the length of the transition segment was extended from 40 mm to 90 mm. Referring to the first modification, the specimens have lower axial force at the same deformation level, since the area of the yielding segment was reduced. As a result, the stress level of the transition segment was lower than that for Series I. With reference to the second modification, the yielding segment near the welds was kept far from the yielding segment, which hinders the development of plastic strains in those regions with significant welding residual stress, further reducing the stress level. Consequently, the main crack for specimen A-V2 was in the yielding segment between the transition segment and the stopper, while that for specimen U-V2 was very close to the stopper, as shown in Fig. 15(e) and (f). Significant reduction of the cross-sectional area was also observed at the center of the core plate of specimen A-V2. As shown in Fig. 15(g), the failure mode for specimen A-V2(3) is similar to that for specimen A-V2, except that the stopper withstood great bending deformation.

4.2.3. Specimens A-C1 and A-C2

The failure mode of specimen A-C2 is the same as that of specimen A-V2, with shrinkage near the stopper and cracks in the yielding segment, as shown in Fig. 15(h). However, the failure mode for specimen A-C1 is similar to that for specimen U-V1, with cracks near the stopper where complex stress state was developed.

4.3. Residual transverse deformation

It is worth noting that the specimens without the unbonding materials witnessed shrinkage in the middle of the core plate, except for specimen A-C1. After the test, the residual transverse dimensions were measured along the yielding segment of the core plate (points A–J in Fig. 16(a) and points A–L in Fig. 17(a)). Since the fabrication tolerances of the core plate were controlled well within 0.2 mm for the width and 0.05 mm for the thickness, the initial average width b and thickness t can be used to calculate the core plate residual transverse deformations. The core plate residual transverse deformations are shown in Figs. 16–18. These

Table 2

Key parameters of the specimens.

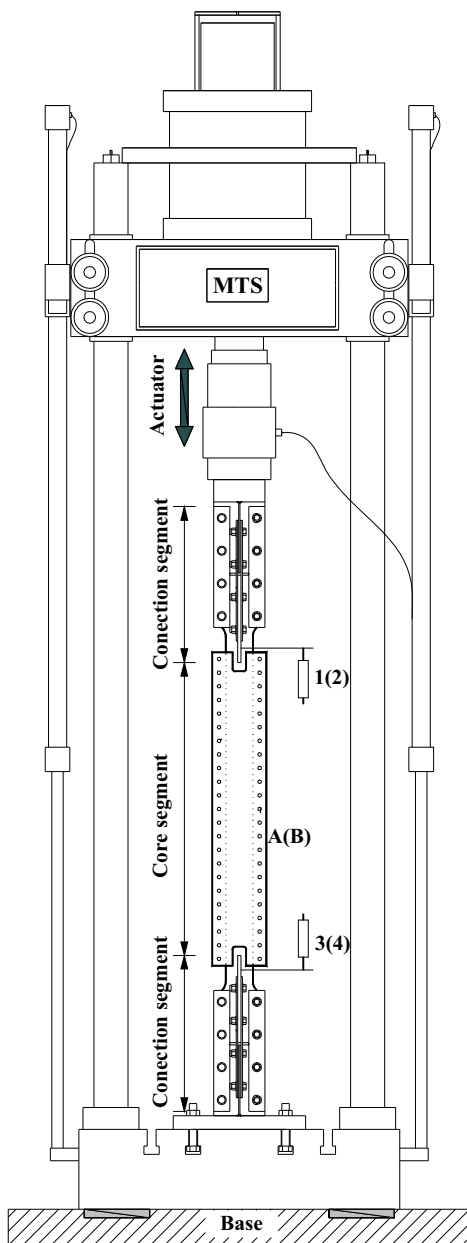
Series	Specimens	L_t (mm)	L_y (mm)	b (mm)	t (mm)	d (mm)	d_0 (mm)	Unbonding materials	Loading pattern
S-I	A-V1	1649.5	897.5	100.12	9.83	1	1	No	V1
	U-V1	1650.0	898.5	100.04	9.77	1	1	Yes	V1
S-II	A-V2	1648.3	879.5	79.93	9.64	1	1	No	V2
	U-V2	1649.3	879.5	79.81	9.68	1	1	Yes	V2
	A-V2(3)	1648.5	879.0	79.84	9.73	1	3	No	V2
	A-C1	1649.0	879.8	79.90	9.66	1	1	No	C1
	A-C2	1649.3	879.3	79.91	9.67	1	1	No	C2

Table 3

Material constants of the core plate.

Series	E (MPa)	σ_y (MPa)	ε_y (%)	σ_u (MPa)	ε_u (%)
S-I	1.92×10^5	253.1	0.132	435.9	36.8
S-II	1.93×10^5	285.1	0.148	462.6	30.8

Note: σ_u and ε_u are the ultimate tensile strength and ultimate strain of the core plate, respectively.

**Fig. 7.** Test setup.

figures indicate that, for the specimens without the unbonding materials, the middle region of the yielding segment shrunk and the end region of the yielding segment expanded considerably, while the residual deformations for the specimens with the unbonding materials were irregular and relatively small. As shown in Fig. 18, the specimen without the unbonding materials with large strain amplitude (specimen A-C2) presented more significant residual transverse deformation compared to that with small strain amplitude (specimen A-C1).

5. Discussions on the test results

5.1. The compression strength adjustment factor β

The experimental β values for all the seven specimens at different CPD values or strain levels are plotted in Figs. 19–21, which give a direct comparison among the specimens.

5.1.1. Specimens A-V1 and U-V1

During the VSA loading, the β value for specimen A-V1 increased from 1.05 at 0.5% to 1.15 at 3.0%, much more sharply than that for specimen U-V1, as shown in Fig. 19. During the CSA loading, the β value for specimen A-V1 increased to the acceptable bound (1.30 specified by AISC 2010 [34]) when CPD capacity reached as far as 2000, and finally to 1.43 as the CPD capacity grew over 3000, while the β value for specimen U-A1 almost remained stable at about 1.09.

5.1.2. Specimens A-V2, U-V2 and A-V2(3)

Among all the three VSA loadings (Fig. 20), the β value for specimen A-V2 was significantly larger than that for specimen U-V2 at strain amplitude over 0.5%, but less than that for specimen A-V2(3). For instance, at CPD value of 1000, the β value for specimens A-V2, U-V2 and A-V2(3) reached 1.42, 1.13 and 1.73, respectively. It is worth noting that the β values for specimens A-V2 and A-V2(3) at a certain strain amplitude increased as the loading history developed from VSA1 to VSA2, while the β value for specimen U-V2 at a certain strain amplitude remained almost the same.

5.1.3. Specimens A-C1 and A-C2

In the first few cycles, the β values for the two specimens were relatively high owing to the cyclic hardening effect, where the cyclic stress amplitude increased considerably with the CSA loading history (e.g., from tension to compression in a loading cycle) until the formation of a static hysteretic loop [36]. After that, the β values for the two specimens both grew up with a little fluctuation, eventually reaching 1.53 for specimen A-C2 and 1.31 for specimen A-C1. In particular, the β value for specimen A-C2 increased more drastically than that for specimen A-C1, as shown in Fig. 21.

The β values for all the seven specimens are below 1.3 even under the CPD value of 600, which is qualified according to AISC 2010, except for the first cycle of specimen A-C1 with cyclic hardening effect. It also indicates that the excessive friction between the core plate and the restraining members can be prevented under three strong earthquakes, which is one of the requirements for high performance BRBs [11,37,38]. Furthermore, the β values for the specimens with and without the unbonding materials show great divergences as the development of the loading history. To figure out the reason, the specimens were split by removing the high strength bolts after the test. Interestingly, the surfaces of the core plates of all the specimens without the unbonding materials were partly polished (Fig. 22(a)–(e)) and the oxygen films on the surfaces were ground off and turned into tiny rust around the high-mode buckling wave crests, while the surfaces of the core plates of the specimens with the unbonding materials were still covered with the unbonding materials and remained dark after removing the unbonding materials (Fig. 22(f)). However, the kinetic coefficient of friction for dry interface between two metals is much higher than that for greasy interface, because of the larger molecular interaction and adhesion on the interface [39]. Taking mild steel-mild steel interface for instance, the kinetic coefficient of friction for greasy interface is 0.09, while that for dry interface is 0.57 [40]. The law is also illustrated in the literature [41] that the coefficient of friction of the greasy interface increases rapidly after reverse intensively rubbing, which is considered to be one of the

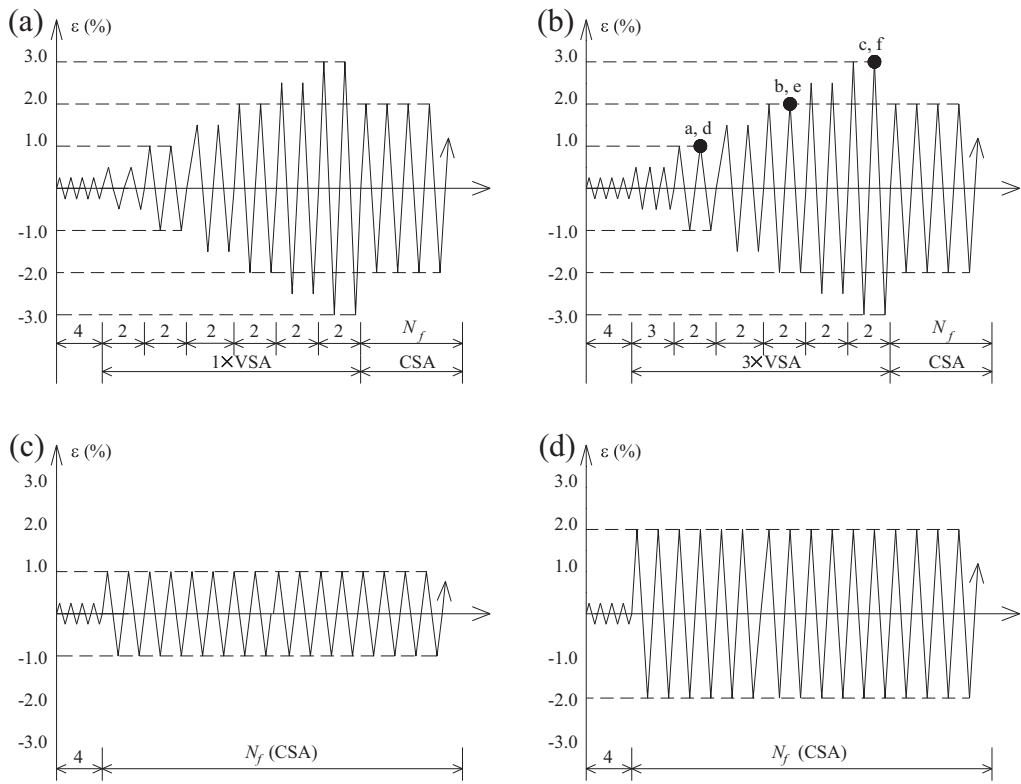


Fig. 8. Loading protocols: (a) V1, (b) V2, (c) C1, (d) C2.

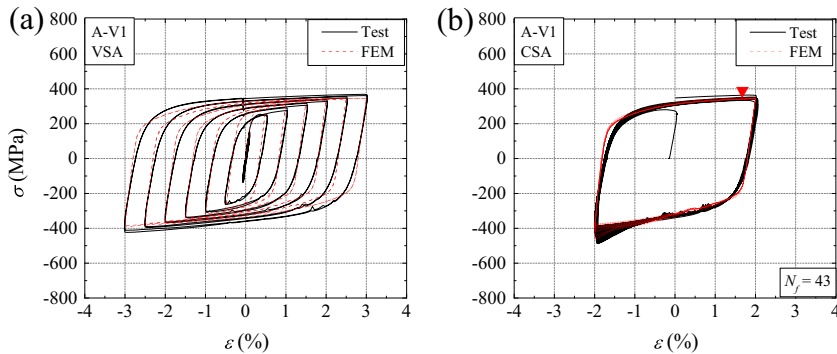


Fig. 9. Stress-strain curve of specimen A-V1: (a) VSA loading, (b) CSA loading.

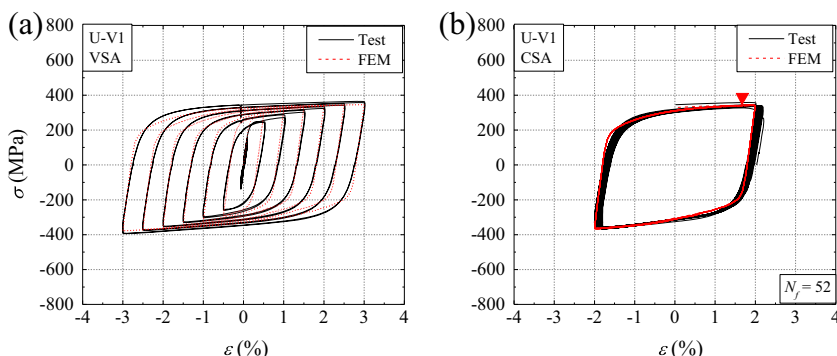


Fig. 10. Stress-strain curve of specimen U-V1: (a) VSA loading, (b) CSA loading.

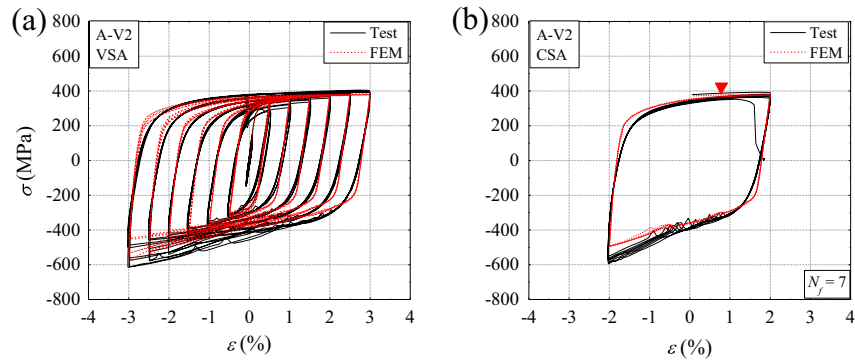


Fig. 11. Stress–strain curve of specimen A-V2: (a) VSA loadings, (b) CSA loading.

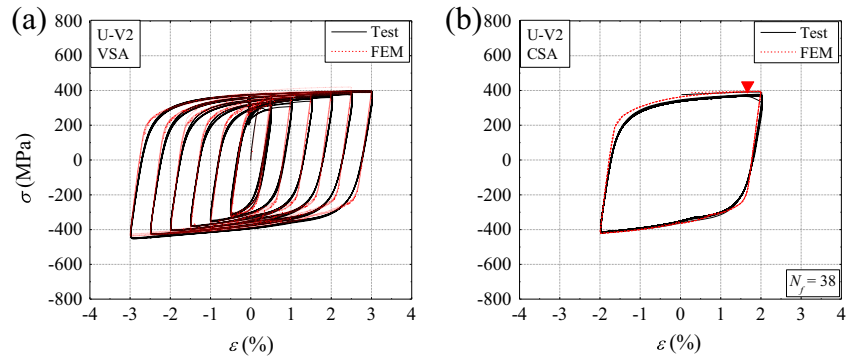


Fig. 12. Stress–strain curve of specimen U-V2: (a) VSA loadings, (b) CSA loading.

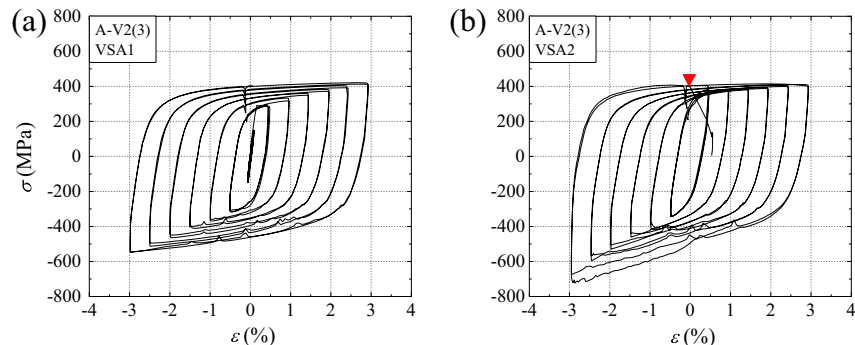


Fig. 13. Experimental stress–strain curve of specimens A-V2(3): (a) VSA1 loading, (b) VSA2 loading.

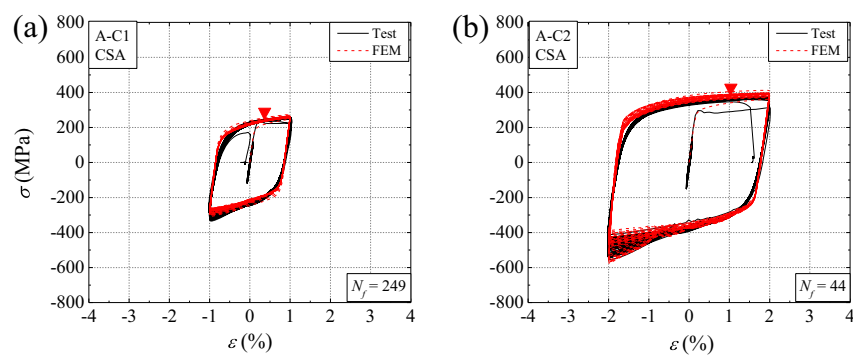


Fig. 14. Stress–strain curves of (a) specimen A-C1 and (b) specimen A-C2.

Table 4

Theoretical weak-axis high-mode buckling and experimental CPD capacities.

Series	Specimens	$\Delta\varepsilon$ (%)	T_{\max} (kN)	N (kN)	l_w (mm)	β (theory)	Δb_{th} (mm)	$2d_0$ (mm)	CPD
S-I	A-V1	2.0	319.7	25.3	128.2	1.27	2.2	2.0	3022
	U-V1	2.0	317.5	21.3	128.4	1.07	1.1	2.0	3532
S-II	A-V2	3.0	304.5	30.4	109.9	1.37	2.8	2.0	2188
	U-V2	3.0	305.3	21.4	125.6	1.09	1.3	2.0	5391
	A-V2(3)	3.0	307.0	28.7	109.9	1.28	2.7	6.0	1058
	A-C1	1.0	245.4	19.5	125.7	1.24	1.3	2.0	5734
	A-C2	2.0	275.5	27.0	109.9	1.34	2.2	2.0	2202

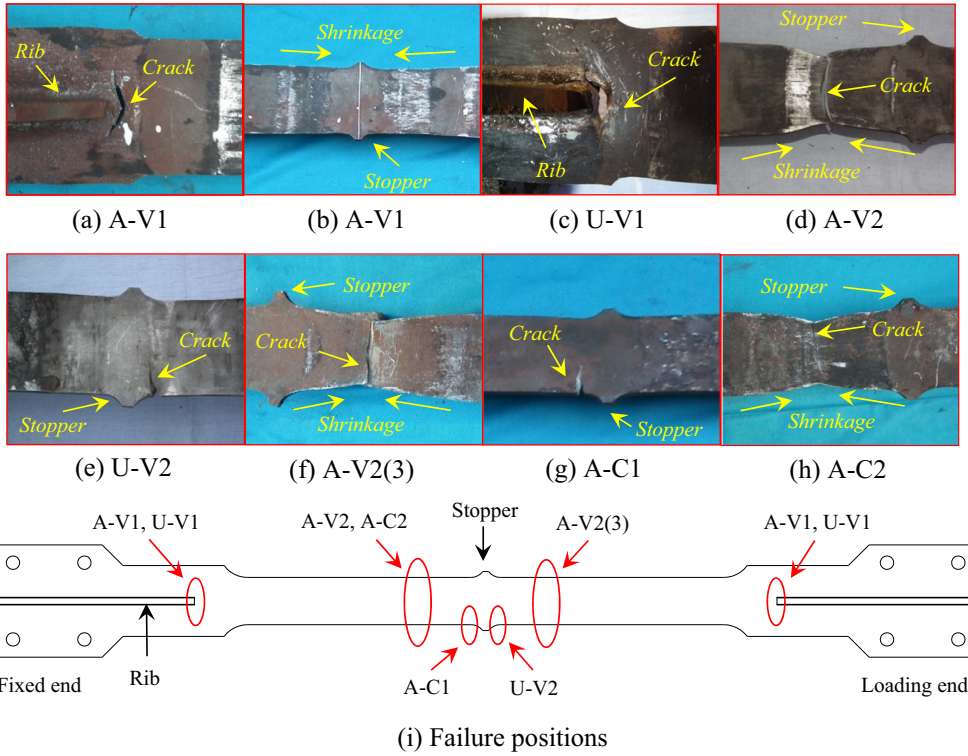


Fig. 15. Failure modes for the seven specimens.

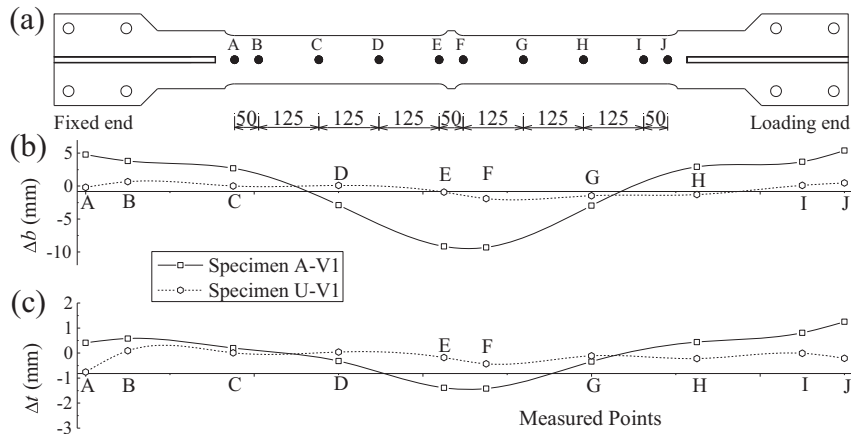


Fig. 16. Core plate residual transverse deformation of specimens A-V1 and U-V1 at the measured points: (a) the position of the measured points for specimens in Series I, (b) in the direction of the width, (c) in the direction of the thickness.

reasons for the drastic increase of the compressive force for the specimens without the unbonding materials in the experiments. Accordingly, the increasing of the coefficient of friction μ is

believed to be mainly influenced by the maximum contact force and the time of the rubbing between the core plate and the restraining members. In order to account for the two factors, each

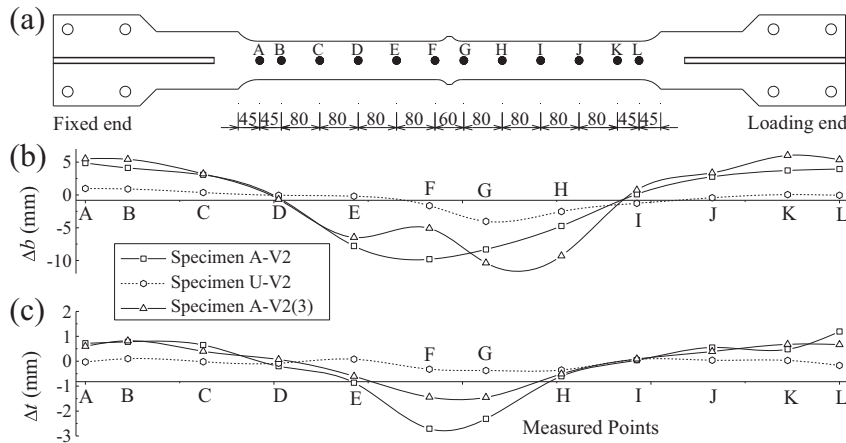


Fig. 17. Core plate residual transverse deformation of specimens A-V2, U-V2 and A-V2(3) at the measured points: (a) the position of the measured points for specimens in Series II, (b) in the direction of the width, (c) in the direction of the thickness.

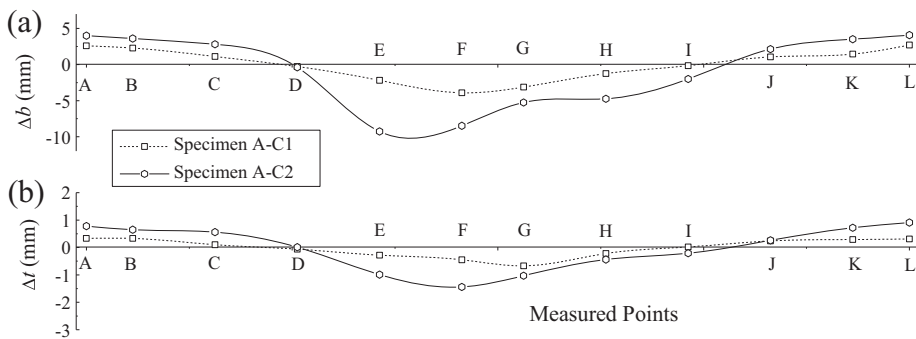


Fig. 18. Core plate residual transverse deformation of specimens A-C1 and A-C2 at the measured points: (a) in the direction of the width, (b) in the direction of the thickness.

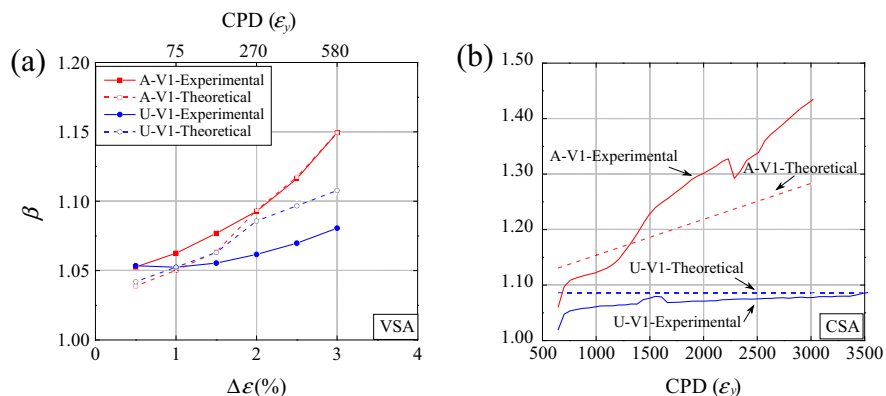


Fig. 19. The experimental and theoretical compression strength adjustment factor β for specimens A-V1 and U-V1 at different strain amplitudes and CPD values.

strain amplitude $\Delta \varepsilon_i$ and the corresponding cycle numbers N_i are employed to describe the change of the coefficient of friction μ with the loading history as:

$$\mu = 0.09 + \sum_i N_i (100 \Delta \varepsilon_i / 3)^{2.6} / 33 \leq 0.57 \quad (9)$$

The formula is chosen under the assumption that the coefficients of friction μ of all the specimens without the unbonding materials are initially 0.09 and could gradually increase to 0.5–0.57 at the end of the loading. In addition, the kinetic coefficient of friction for the specimens with the unbonding materials (butyl rubber) is set as 0.1 [33].

With the above kinetic coefficients of friction, the theoretical β values for all the seven specimens estimated via Eqs. (3) and (7) are also plotted in Figs. 19–21. The trends of all the theoretical β values in terms of the strain amplitudes and CPD values are consistent with the experimental values. For the specimens with the unbonding materials, the percent difference between the theoretical and experimental β values is below 5% except at the strain amplitude of 0.5%, and tends to increase with the strain amplitude, as shown in Fig. 20. However, for the specimens without the unbonding materials, the percent difference between the theoretical and experimental β values is much larger, but also tends to increase with both the strain amplitude and the loading history.

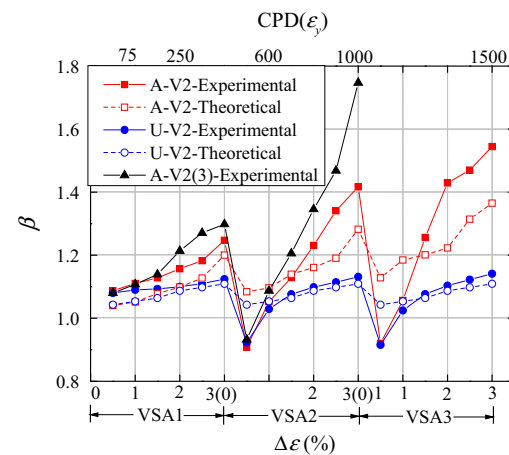


Fig. 20. The experimental and theoretical compression strength adjustment factor β for specimens A-V2, U-V2 and A-V2(3) at each strain level and different CPD values.

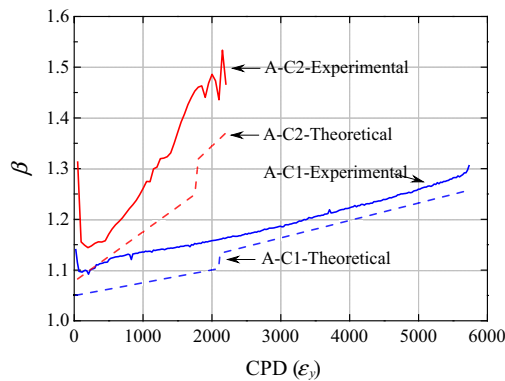


Fig. 21. The experimental and theoretical compression strength adjustment factor β for specimens A-C2 and A-C1 at different CPD values.

Besides, less difference between the theoretical and experimental β values is shown for specimen A-C1 with a low constant strain amplitude, compared to specimen A-C2 with a high constant strain amplitude.

5.2. Jamming between the core plate and the restraining members

The significant difference between the theoretical and experimental β values for specimens without the unbonding materials is considered to be largely attributed to the expansion of the width of the core plate (Fig. 23), which exceeded two times the in-plane gap width d_0 between the yielding segment and the filler verified by the residual deformation observed after the test. The theoretical expansion of the width of the core plate Δb_{th} caused by the Poisson's effect and the friction force can be predicted as:

$$\Delta b_{th} = v \left(\Delta \varepsilon + \frac{P_{f,max}}{E_t b t} \right) b \quad (10)$$

$$P_{f,max} = \sum_n f_{max} = n \mu P_{max} \frac{8d}{l_w} \quad (11)$$

where v is the Poisson's ratio, and $P_{f,max}$ is the maximum total friction force induced by the weak-axis high-mode buckling. f_{max} is the maximum friction force in each discrete contact region induced by the weak-axis high-mode buckling. Theoretical values of the expansion of the width of the core plate Δb_{th} at certain strain amplitudes calculated by Eq. (10) and the theoretical compression strength adjustment factor β are listed in Table 4, together with the theoretical values of weak-axis wavelength l_w and the normal contact force N . If the expansion of the width Δb_{th} calculated by Eq. (10) is larger than two times the gap width provided between the core plate and the restraining members, the friction force will increase sharply and the compression strength adjustment factor will outnumber significantly the theoretical values. That is the case for specimens A-V1, A-V2 and A-C2 referred to Table 4 and Figs. 18–20. Though it is designed that the in-plane gap width between the yielding segment and the filler d_0 of specimen A-V2(3) is 3 mm, which provides sufficient expansion space, the in-plane gap width between the transition segment (also yielding during test) and the filler d_1 is designed as only 1 mm (Fig. 6). Moreover, the stopper of specimen A-V2(3) failed during the test, on account of the smaller flexural stiffness (Fig. 6) compared to the other specimens, which caused the maximum compressive force to further increase [33].

5.3. Cumulative strain concentration along the core plate

It is illustrated in Fig. 24 that the deformation of the core plate for the specimens without the unbonding materials during each

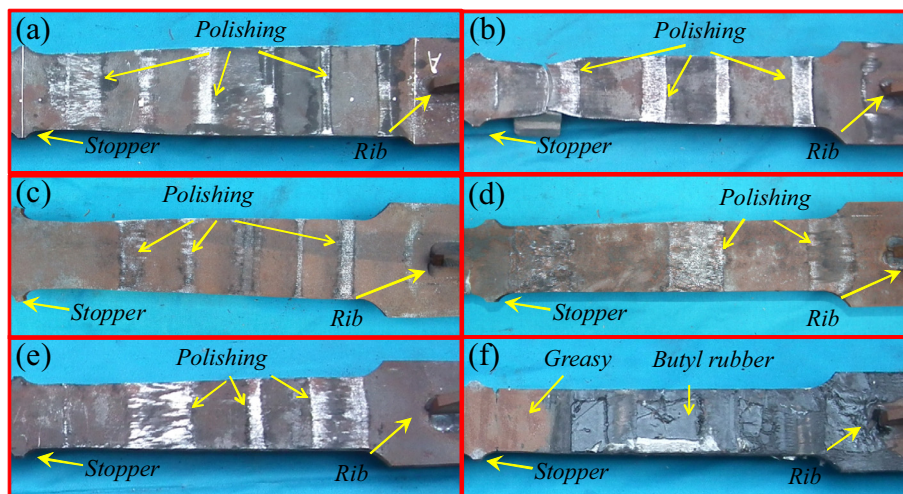


Fig. 22. The surface of core plates after the test for specimen: (a) A-V1, (b) A-V2, (c) A-V2(3), (d) A-C1, (e) A-C2, (f) U-V2.

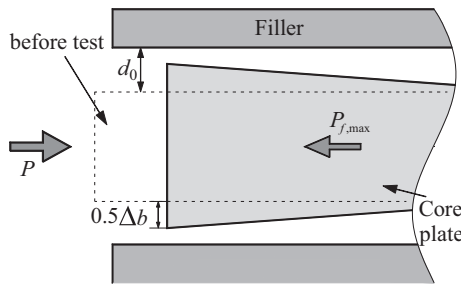


Fig. 23. The expansion of the width of the core plate.

stage of loadings. Under compression, the axial force in the end of the yielding segment P_e was larger than the axial force in the middle P_m , for that the direction of the friction force of the core plate imposed by the restraining member is from the middle to the two ends. Since the cross-sectional area of the yielding segment originally remained the same along the longitudinal direction, the distribution of the normal stress along the longitudinal direction kept consistent with the distribution of the axial force, i.e., $|\sigma_m| < |\sigma_e|$, where σ_m and σ_e are the stress in the middle and end portion of the yielding segment, respectively. At the plastic stage, small difference in the stress makes significant difference in the strain, so the end of the yielding segment expanded more considerably than the middle at the end of the compression, as shown in Fig. 24(b). Under tension, the axial force in the core plate was uniform along the longitudinal direction, which was equal to the applied tensile force of the actuator, i.e., $T_m = T_e$. However, larger tensile stress was generated in the middle ($|\sigma_m| > |\sigma_e|$) owing to the smaller cross-sectional area of the core plate after compression, which also caused strain concentration in the middle, as shown in Fig. 24(c) and (d). Hence, the middle region of the yielding segment developed more transverse deformation under tension. As a consequence, strain concentration along the core plate was accumulated under reverse compression and tension, finally forming the residual transverse deformation for the specimens without the unbonding materials as shown in Figs. 16–18. Since the specimens without the unbonding materials demonstrated larger strain concentration both in tension and compression, their CPD capacities are not so high as the CPD capacities for the specimens with the unbonding materials under the same loading protocol, as listed in Table 4.

6. Numerical study

6.1. Finite element models

Numerical simulations of BRBs using ABAQUS [17] program were conducted to predict the β value and the high-mode buckling

responses. Fig. 25 illustrates the finite element model (FEM) for the specimens. The specimen's core plate was modeled with the four-node shell elements, and the restraining members were modeled with the eight-node solid elements. Before loading, the restraining plates and the filler were connected by the tightened high strength bolts. Nonlinear isotropic/kinematic hardening model with multiple backstresses was employed for the material properties. Besides, the 'hard contact' interface property was specified on the surfaces between the core plate and the restraining members, allowing the normal force and the friction to develop between the surfaces. The Coulomb friction model was employed to simulate the tangential behavior between the restraining members and the core plate for specimens both with and without the unbonding materials, the coefficients of friction of which were set the same as those in Section 5.1.

The off-plumb imperfection of the core plate was considered as the first mode buckling wave shape with a peak magnitude of 1/1000 of the length of the yielding segment in the finite element model. Since the ribs and the end region of the core plate would remain elastic during the loading, only the yielding segment and the transition segment of the core plate were included in the finite element model for simplification. The load was applied at both ends of the transition segment according to the displacement histories in Fig. 8, by constraining the end nodes to move only in the longitudinal direction without any other transition or rotation.

6.2. Numerical results

The finite element analysis results are plotted in Figs. 9–12 and 14, in comparison with the experimental hysteresis loops except for specimen A-V2(3). It is indicated that the numerical elastic stiffness and hysteresis response keep in good agreement with the experimental values. Moreover, the numerical model can predict the asymmetric behavior well even for the specimens without the unbonding materials. In addition, plastic strain was also developed considerably in the transition segment as expected.

It is demonstrated in Fig. 26 that the normal contact stress envelope on both sides of the core plate imposed by the restraining members at different loading stages for specimen A-V2. The stages correspond to points 'a' to 'f' in Fig. 8(b), where 'a', 'b' and 'c' are the maximum compressive strain stage at the strain amplitude of 1.0%, 2.0% and 3.0% during the VSA1 loading phase, respectively, and 'd', 'e' and 'f' are the maximum compressive strain stage at the strain amplitude of 1.0%, 2.0% and 3.0% during the VSA2 loading phase, respectively. As the strain amplitude grew from stage 'a' to 'b' or 'd' to 'e', the contact stress increased considerably and the wavelength reduced slightly. When the strain amplitude further increased from stage 'b' to 'c' or 'e' to 'f', significant high contact press could be observed at both ends of the core plate, which

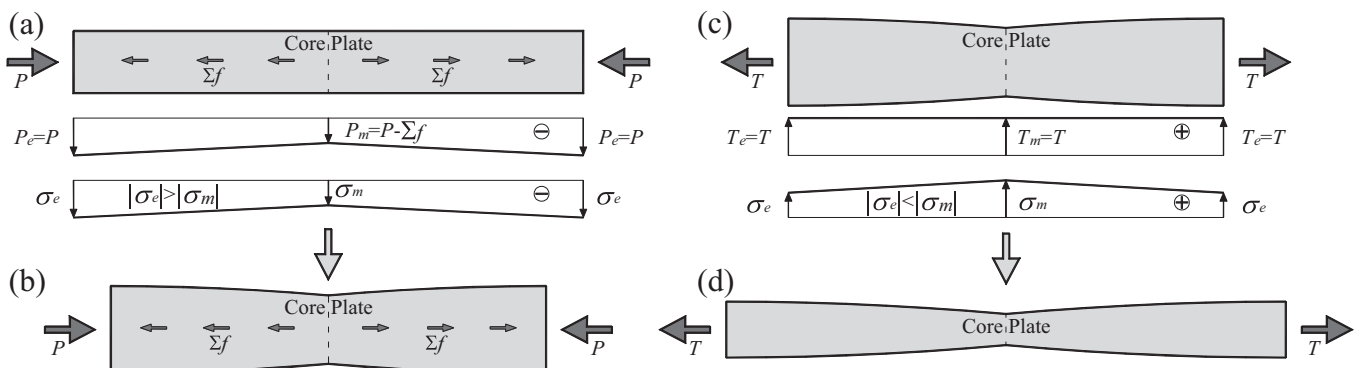


Fig. 24. Core plate deformation and axial force: (a) at the beginning of compression, (b) at the end of compression, (c) at the beginning of tension, (d) at the end of tension.

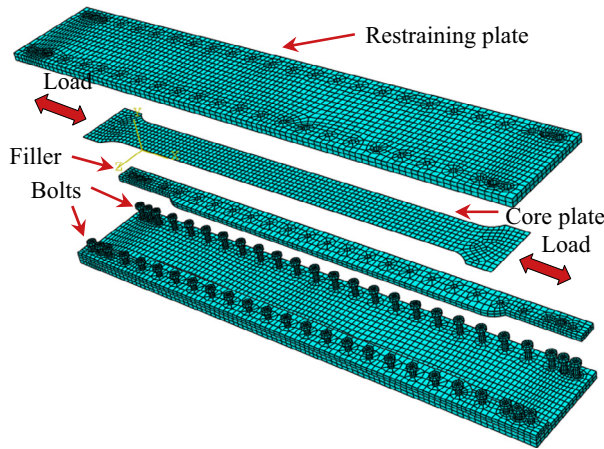


Fig. 25. Finite element model of the specimen.

Table 5
Parameters and results of numerical models.

BRB models	L_y (mm)	t (mm)	d_0 (mm)	β	
				(CPD = 200)	(CPD = 600)
A	U	A	U		
880-10	880	10	1.5	1.07	1.07
3000-10	3000	10	2.5	1.18	1.14
6000-10	6000	10	5.0	1.35	1.28
6000-15	6000	15	5.0	1.18	1.14
6000-30	6000	20	5.0	1.11	1.11

Note: β values in the parentheses are for the BRB models with the unbonding materials. 'A' and 'U' stand for the air-gap and the unbonding materials employed in each BRB models, respectively.

indicates that the width of the core plate expanded beyond the provided space as described in Section 5.2. It is noted that the axial compressive force experienced a sharp increase at the time step when the core plate expanded to squeeze the fillers, which validates the reason for the increasing axial compressive force as

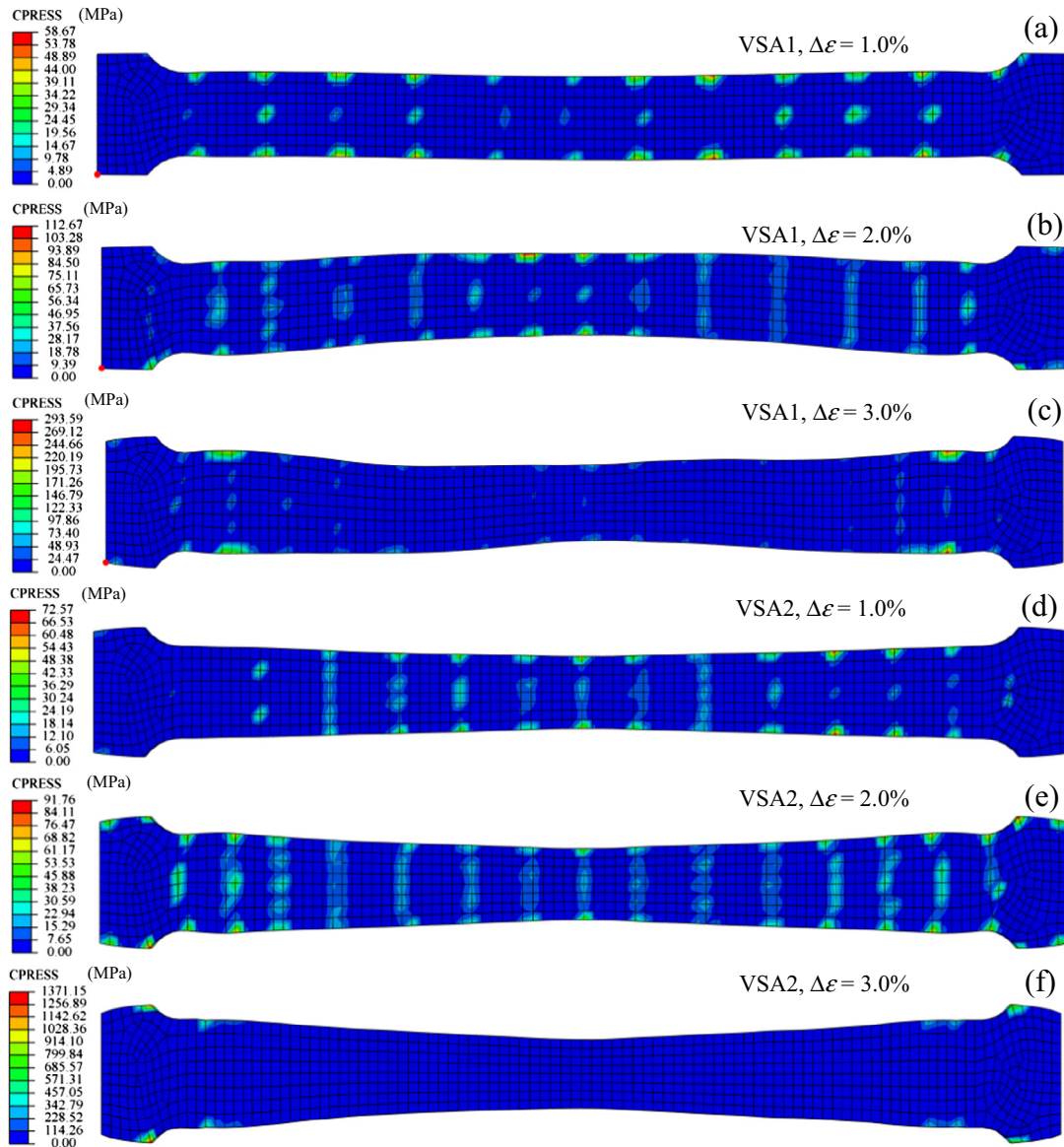


Fig. 26. Contact stress envelope on both sides of the core plate for specimen A-V2; displacement in the direction of the width magnified by a factor of 10.

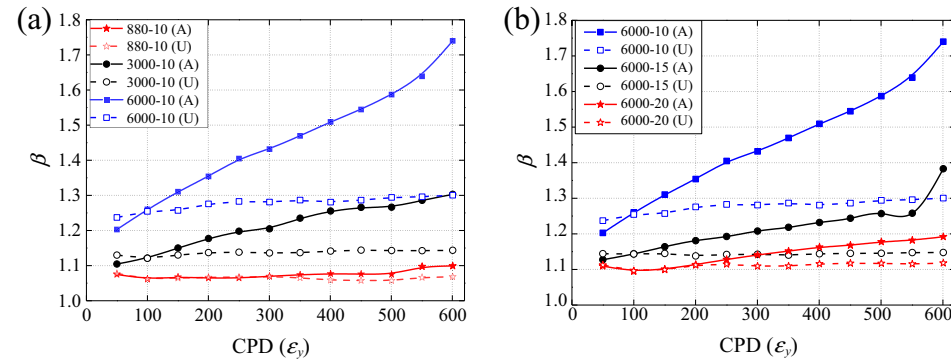


Fig. 27. The compression strength adjustment factor β for analytical BRB models at different CPD values (a) with varied lengths of the yielding segment L_y , (b) with varied thicknesses of the yielding segment t . Note: 'A' and 'U' in the parentheses stand for the air-gap and the unbonding materials employed in each BRB models, respectively.

mentioned in Section 5.2. Moreover, it is also observed that the end portion of the core plate expanded and the middle portion shrunk as described in Section 4.3, especially for stage 'c' and 'f' with large strain amplitude. More strain concentration in the end and middle of the core plate was detected at the same strain amplitude during the VSA2 loading than that during the VSA1 loading, when comparing stages 'd'–'f' with stages 'a'–'c'. By contrast, much less strain concentration along the longitude direction was observed in the numerical results of specimen U-V2.

6.3. Influence of key parameters

Though specimen A-V2(3) was designed with sufficient in-plane gap width to avoid the jamming between the filler and the yielding segment of the core plate, extremely high β value was demonstrated during the test because of weak stopper and small in-plane gap width between the filler and the transition segment of the core plate. However, it is still believed that the undesirable jamming between the core plate and the filler could be avoided by increasing the in-plane gap width and proper design of the stopper. Notwithstanding large in-plane gap width may weaken the low-cycle fatigue properties of the specimen due to significant strong-axis buckling, researches have shown that the decline of the low-cycle fatigue properties is acceptable even for a specimen with in-plane gap width of 6 mm [4]. Hence, the in-plane gap width d_0 was designed to be moderately over half of the expansion of the width of the core plate Δb_{th} in the following models of BRBs (Table 5).

The tests have shown that all the specimens meet standard requirements well even beyond CPD capacities of 600, but the length of the yielding segment of BRBs in engineering practice is generally much longer than that of the tested specimens. To evaluate the influence of the length of the yielding segment L_y , parameter studies were performed on BRBs with or without the unbonding materials using numerical models. Three different L_y values were employed for BRB models (880–10, 3000–10, 6000–10 as listed in Table 5) with and without the unbonding materials, and the applied loading pattern is 'C2' described in Fig. 8. The cross section of the BRB models was the same as that of specimens in Series II, except for larger in-plane gap width. The β values for the six BRB models with respect to different CPD values are plotted in Fig. 27(a). In accordance with Eq. (7), BRB models with longer yielding segment present higher β values, the reason for which is that the number of high-mode wave n is positively correlated to the length of the yielding segment L_y . Numerical results have shown that buckling wavelength for BRB models with L_y of 6000 mm is close to the upper bounds in Eq. (2), for line contact regions are less likely to concentrate in certain wave crests compared to BRBs with L_y of 880 mm. The difference between

the β values for BRB models with and without the unbonding materials also increases significantly with the growth of the length of the yielding segment.

In practice, a great number of thicknesses have been employed for the core plate. Previous study has shown that the thickness of the core plate t has a significant influence on the buckling behavior and the contact force [42]. Therefore, the effect of the thickness of the core plate t on the β values was investigated for BRB models (6000–10, 6000–15, 6000–20 as listed in Table 5) with L_y of 6000 mm, as shown in Fig. 27(b). To the contrary, the β values show a negative correlation with the thickness of the core plate, as well as the difference between the β values for BRB models with and without the unbonding materials. Referring to Eq. (1), fewer numbers of high-mode wave n and longer wavelength l_w are expected for BRB models with larger thickness of the core plate, and thus smaller friction force was developed between the core plate and the restraining members.

The β values for all the BRB models, except for the one with $L_y = 6000$ mm and $t = 10$ mm, are within the code limit (1.3) at the CPD value of 200 (Table 5), which indicates that the unbonding materials are not necessary for these all-steel BRBs without introducing significant asymmetric behavior. However, for high performance BRBs designed to suffer three major earthquakes [37], the β values could reach 1.3 with L_y not less than 3000 mm or t not less than 15 mm, in the absence of the unbonding materials at the CPD value of 600. Specially, the BRB model with $L_y = 6000$ mm and $t = 10$ mm demonstrates extremely high β value (1.74) at the CPD value of 600, provided the unbonding materials is not employed.

In addition, joint rotations and the type of connection at BRB ends generally affect significantly the response of BRBs [20,43,44]. Therefore, sub-assemblages tests and corresponding numerical studies need to be conducted to further investigate the influence of the unbonding materials in the future.

7. Conclusions

- (1) To evaluate the effect of the unbonding materials in all-steel BRBs, seven BRB specimens were designed and tested. These specimens all exhibited excellent energy absorption performance with the CPD capacities of 3022, 3532, 2188, 5391, 1058, 5734 and 2202 for specimens A-V1, U-V1, A-V2, U-V2, A-V2(3), A-C1 and A-C2, respectively. Further, the specimens with the unbonding materials demonstrated higher low-cycle fatigue properties against the specimens without the unbonding materials.
- (2) Compared to the specimens with the unbonding materials, significantly larger compression strength adjustment factor β was developed in the specimens without the unbonding

- materials. It is owing to gradually increasing coefficient of friction and the jamming between the end of the core plate and the restraining members. Nevertheless, the β values for all the seven specimens are almost below the code limit 1.3 even under the CPD value of 600.
- (3) After reducing the cross-sectional area of the yielding segment, unfavorable failure near the welds in the end (observed in Series I) was avoided in the test of Series II. The specimens without the unbonding materials except for specimen A-C1 witnessed shrinkage in the middle and expansion in the end after the test, which is caused by gradually accumulated strain concentration along the core plate under reverse compression and tension.
- (4) Theoretical formula to predict the compression strength adjustment factor was proposed based on the high-mode buckling behavior of the core plate, which is in agreement with the specimens with the unbonding materials. However, the discrepancy between the theoretical and experimental β value is considerable for the specimens without the unbonding materials (except for specimen A-C1), due to the jamming between the core plate and the restraining members, where the core plate expanded beyond the provided gap in the end.
- (5) The hysteresis responses of the specimens can be simulated rather well with the proposed finite element model. Moreover, the finite element model can exhibit nonuniform deformation distribution and the jamming between the core plate and the restraining members well in accordance with the experiment results. Based on the numerical results, the compression strength adjustment factor β is positively related with the yielding length of the core plate, while it is negatively related with the thickness of the core plate.
- (6) Both the experimental and numerical results have shown that the β values can be controlled beyond code limit at the CPD value of 200 even without employing the unbonding materials, which indicates that the unbonding materials are not essential in most all-steel BRBs. But for high performance BRBs with long yielding segment and thin core plate, the unbonding materials are still necessary, so as to get higher low-cycle fatigue properties and avoid significant great β values at larger CPD values.

Acknowledgements

The authors would like to acknowledge financial supports from National Natural Science Foundation of China (51008077, 51278105), Natural Science Foundation of Jiangsu Province of China (BK20151407), A Project Funded by the Priority Academic Program Development of Jiangsu Higher Education Institutions.

References

- [1] Tremblay R, Timler P, Bruneau M, Filiatrault A. Performance of steel structures during the 1994 Northridge earthquake. *Can J Civ Eng* 1995;22:338–60.
- [2] Black CJ, Makris N, Aiken ID. Component testing, stability analysis and characterization of buckling-restrained unbonded braces. Berkeley: Pacific Earthquake Engineering Research Center, University of California; 2002.
- [3] Wang C-L, Usami T, Funayama J, Imase F. Low-cycle fatigue testing of extruded aluminium alloy buckling-restrained braces. *Eng Struct* 2013;46:294–301.
- [4] Wang C-L, Usami T, Funayama J. Improving low-cycle fatigue performance of high-performance buckling-restrained braces by toe-finished method. *J Earthq Eng* 2012;16:1248–68.
- [5] Zhao JX, Wu B, Ou JP. Global stability design method of buckling-restrained braces considering end bending moment transfer: discussion on pinned connections with collars. *Eng Struct* 2013;49:947–62.
- [6] Wu J, Liang RJ, Wu ZS. Matching relationship between axial stiffness and yield strength of buckling restrained braces. *J Earthq Tsunami* 2011;5:71–82.
- [7] Tsai K-C, Hsiao P-C. Pseudo-dynamic test of a full-scale CFT/BRB frame—Part II: Seismic performance of buckling-restrained braces and connections. *Earthq Eng Struct Dynam* 2008;37:1099–115.
- [8] Tsai K-C, Hsiao P-C, Wang K-J, Weng Y-T, Lin M-L, Lin K-C, Chen C-H, Lai J-W, Lin S-L. Pseudo-dynamic tests of a full-scale CFT/BRB frame—Part I: Specimen design, experiment and analysis. *Earthq Eng Struct Dynam* 2008;37:1081–98.
- [9] Sabelli R, Mahin S, Chang C. Seismic demands on steel braced frame buildings with buckling-restrained braces. *Eng Struct* 2003;25:655–66.
- [10] Fahnestock LA, Sause R, Ricles JM. Seismic response and performance of buckling-restrained braced frames. *J Struct Eng, ASCE* 2007;133:1195–204.
- [11] Chen X, Ge HB, Usami T. Seismic demand of buckling-restrained braces installed in steel arch bridges under repeated earthquakes. *J Earthq Tsunami* 2011;5:119–50.
- [12] Wakabayashi M, Nakamura T, Katagihara A, Yogoyama H, Morisono T. Experimental study on the elastoplastic behavior of braces enclosed by precast concrete panels under horizontal cyclic loading – Parts 1 & 2. Kinki Branch of Architectural Institute of Japan; 1973.
- [13] Tsai K-C, Lai J-W, Hwang Y-C, Lin S-L, Weng C-H. Research and application of double-core buckling restrained braces in Taiwan. Presented at the 13th world conference on earthquake engineering, Vancouver, B.C., Canada; 2004.
- [14] Tsai K-C, Wu A-C, Wei C-Y, Lin P-C, Chuang M-C, Yu Y-J. Welded end-slot connection and debonding layers for buckling-restrained braces. *Earthq Eng Struct Dynam* 2014;43:1785–807.
- [15] Palazzo G, López-Almansa F, Cahis X, Crisafulli F. A low-tech dissipative buckling restrained brace. Design, analysis, production and testing. *Eng Struct* 2009;31:2152–61.
- [16] Miller DJ. Development and experimental validation of self-centering buckling-restrained braces with shape memory alloy. Master, University of Illinois at Urbana-Champaign; 2011.
- [17] Wu A-C, Lin P-C, Tsai K-C. High-mode buckling responses of buckling-restrained brace core plates. *Earthq Eng Struct Dynam* 2014;43:375–93.
- [18] Genna F, Gelfi P. Analysis of the lateral thrust in bolted steel buckling-restrained braces. Part I: Experimental and numerical results. *J Struct Eng* 2012;138:1231–43.
- [19] Chou C-C, Chen S-Y. Subassemblage tests and finite element analyses of sandwiched buckling-restrained braces. *Eng Struct* 2010;32:2108–21.
- [20] Della Corte G, D'Aniello M, Landolfo R. Field testing of all-steel buckling-restrained braces applied to a damaged reinforced concrete building. *J Struct Eng* 2015;141:D4014004.
- [21] Iwata M. Applications-design of buckling restrained braces in Japan. Presented at the 13th world conference on earthquake engineering, Vancouver, B.C., Canada; 2004.
- [22] Tremblay R, Bolduc P, Neville R, DeVall R. Seismic testing and performance of buckling-restrained bracing systems. *Can J Civ Eng* 2006;33:183–98.
- [23] Usami T, Ge HB, Kasai A. Overall buckling prevention condition of buckling-restrained braces as a structural control damper. Presented at the 14th world conference on earthquake engineering, Beijing, China; 2008.
- [24] Takeuchi T, Hajjar JF, Matsui R, Nishimoto K, Aiken ID. Local buckling restraint condition for core plates in buckling restrained braces. *J Constr Steel Res* 2010;66:139–49.
- [25] Timoshenko SP, Gere JM. Theory of elastic stability. New York: McGraw-Hill; 1963.
- [26] Chai H. The post-buckling response of a bi-laterally constrained column. *J Mech Phys Solids* 1998;46:1155–81.
- [27] Shanley FR. Inelastic column theory. *J Aeronaut Sci* 1947;14:261–7.
- [28] Wang C-L, Li T, Chen Q, Wu J, Ge HB. Experimental and theoretical studies on plastic torsional buckling of steel buckling-restrained braces. *Adv Struct Eng* 2014;17:871–80.
- [29] Genna F, Gelfi P. Analysis of the lateral thrust in bolted steel buckling-restrained braces. Part II: Engineering analytical estimates. *J Struct Eng* 2012;138:1244–54.
- [30] Wu J, Liang RJ, Wang C-L, Ge HB. Restrained buckling behavior of core component in buckling-restrained braces. *Int J Adv Steel Constr* 2012;8:212–25.
- [31] Lai J-W, Tsai K-C. Research and application of buckling restrained braces in Taiwan. Presented at the ANCER annual meeting, Honolulu, Hawaii, USA; 2004.
- [32] Midorikawa M, Asari T, Iwata M, Murai M, Tanaka Y. Cyclic behaviour of buckling-restrained braces using steel mortar planks; buckling mode number and strength ratio. Presented at the proceedings of the 15th world conference on earthquake engineering, Lisbon, Portugal; 2012.
- [33] Wang C-L, Usami T, Funayama J. Evaluating the influence of stoppers on the low-cycle fatigue properties of high-performance buckling-restrained braces. *Eng Struct* 2012;41:167–76.
- [34] AISC. Seismic provisions for structural steel buildings. Chicago, Illinois; 2010.
- [35] Ge HB, Kang L. Ductile crack initiation and propagation in steel bridge piers subjected to random cyclic loading. *Eng Struct* 2014;59:809–20.
- [36] Broom T, Ham RK. The hardening and softening of metals by cyclic stressing. *Proc Roy Soc Lond Ser A, Math Phys Sci* 1957;242:166–79.
- [37] Usami T, Sato T, Kasai A. Developing high-performance buckling-restrained braces. *J Struct Eng, JSCE* 2009;55A:719–29 [in Japanese].
- [38] Ge HB, Hioki K, Usami T. Demand of seismic brace dampers installed in steel arch bridges. *J Earthq Eng, JSCE* 2005 [in Japanese].
- [39] Bowden RP, Hungries TP. The friction of clean metals and the influence of adsorbed gases. The temperature coefficient of friction. *Proc Roy Soc A* 1939;172:263–79.

- [40] Barrett RT. Fastener design manual. Cleveland (Ohio): Lewis Research Center; 1990.
- [41] Rabinowicz E. Friction and wear of materials. 2nd ed. New York: Wiley; 1965.
- [42] Jiang ZQ, Guo YL, Zhang BH, Zhang XQ. Influence of design parameters of buckling-restrained brace on its performance. *J Constr Steel Res* 2015;105:139–50.
- [43] Jia MM, Lu DG, Guo LH, Sun L. Experimental research and cyclic behavior of buckling-restrained braced composite frame. *J Constr Steel Res* 2014;95:90–105.
- [44] Zhao JX, Wu B, Ou JP. Flexural demand on pin-connected buckling-restrained braces and design recommendations. *J Struct Eng* 2012;138:1398–415.